Received: 23 May 2023 | Revised: 18 July 2023 | Accepted: 27 July 2023

DOI: 10.1002/cjce.25066

RESEARCH ARTICLE

THE CANADIAN JOURNAL OF CHEMICAL ENGINEERING

Free-energy lattice Boltzmann simulations of slicing of rising droplets

Jiawei Cao[1] | **Fengjiao Liu**[1] | **Shipeng Wang**[1] | **Xiang Li**[1] | **Lijuan Zhang**[1] | **Jie Lu**[1] | **Jos J. Derksen**[2]

[1]School of Chemistry and Chemical Engineering, Shanghai University of Engineering Science, Shanghai, China

[2]School of Engineering, University of Aberdeen, Aberdeen, UK

Correspondence
Fengjiao Liu, School of Chemistry and Chemical Engineering, Shanghai University of Engineering Science, Shanghai, China.
Email: fjliu@sues.edu.cn

Jie Lu, School of Chemistry and Chemical Engineering, Shanghai University of Engineering Science, Shanghai, China.
Email: lujie@sues.edu.cn

Funding information
National Natural Science Foundation of China, Grant/Award Numbers: 21978165, 22078191, 92156020; Shanghai Sailing Program, Grant/Award Number: 20YF1416000

Abstract

We performed two-dimensional simulations of the slicing of a rising droplet by a vertical knife and by two knives. We used a free-energy lattice Boltzmann method. Most simulations are for an Eötvös number of 3.96 and a Morton number of 1.24×10^{-4}. We carefully probed effects of the spatial resolution on the rising speed and slicing process. The effect of wettability of the knife(s) was studied by varying the equilibrium contact angle of the drop on the knife in the range of 45° to 135°. Slicing time as well as fine droplet fragments staying behind on the knife depend on the knife's wettability.

KEYWORDS

contact angle, droplet slicing, free energy model, lattice Boltzmann, rising droplet

1 | INTRODUCTION

There are many natural and technological examples where liquid droplets are dispersed in a continuous fluid. In engineered systems the droplet size or—better—the droplet size distribution is an important process parameter. For example, in the production of inhalers,[1] careful control of droplet size is necessary to ensure effective delivery of medication to the lungs. Additionally, in spray drying,[2] smaller droplets can result in faster drying times, higher yields, and reduced production costs. In agriculture, optimizing spray coverage and penetration of pests[3] and weeds[4] may be achieved through controlling droplet size and distribution. Whether it is delivering medication to the lungs or optimizing spray coverage, careful consideration of droplet size is crucial for efficient and effective production.

In recent years, there has been an increasing amount of research on the collision of droplets with solids with different surface properties. In terms of numerical simulation, Raman et al.[5] simulated droplet impact on solid substrates and found that the gradient wetting solid induced directional behaviour of impacting droplets. Tembely et al.[6] found that the wetting properties of the solid matrix impacted by droplets affect the evolution of droplet spreading diameter. Tilehboni et al.[7] found that droplets do not separate from hydrophilic walls at low Eötvös numbers (Eo ≤ 6), but separate from the wall in the total range of Eötvös numbers examined on hydrophobic walls. Additionally, Ma et al.[8] used the lattice Boltzmann method (LBM) to simulate the impact process of oversaturated fuel droplets on inclined blade surfaces in superheated gas, and found that impact angle, surface wetting properties, and Weber number influence droplet deformation and evaporation. The effect of impact angle on droplet velocity was more significant than other factors. Liang et al.[9] studied the impact of

droplets on hydrophilic or hydrophobic pore surfaces and found that at lower Weber numbers, droplets are not easily passed through the pore, and liquid plugs are formed in hydrophilic pores due to capillary action on the pore surface. At high Weber numbers, droplets would break when impacting the pore plate. In the field of experimental research, Abubakar et al.[10] conducted an experimental study of the effect of droplet diffusion on the wetting state of a hydrophobic surface. Liu et al.[11] found that when the impact velocity of a droplet is constant, an increase in the surface hydrophobicity value is detrimental to the spreading of the liquid film across the tubular surface. The larger the surface contact angle, the greater the likelihood of droplet rebound. Naveen et al.[12] investigated the morphology and diffusion phenomena of water droplet collisions on hydrophilic, hydrophobic, and superhydrophobic surfaces and found that some differences exist. By simulating or experimenting with the effects of collisions of droplets on different wettable surfaces and a variety of other factors, it was found that wettability plays an important role in the spreading of droplets and changes in contact angle.

There is a strong connection between experimental work on droplet collisions and numerical simulations. Experimental work can provide valuable insights into the behaviour of droplet collisions and experimental results can be used to verify and validate simulation models. Simulations can help to analyze the complex physical phenomena involved in droplet collisions. It can be used to improve the experimental setup and to obtain more accurate and reliable data. The impact of a droplet on a solid surface is a highly dynamic process involving the deformation of the droplet, the rebound or deposition of the droplet, and the angle of contact between the droplet and the solid surface.[13–17] To accurately capture the details of this process in numerical simulations requires high resolution and careful consideration of the relevant physical phenomena. The properties of the solid surface, such as the wettability[18,19] and chemical composition,[20–22] greatly influence the behaviour of droplets on its surface. Capturing these effects in numerical simulations requires accurate modelling of surface properties.

We study the cutting behaviour of binary systems, focusing in particular on the slicing of clean droplets. However, it is important to consider the potential influence of surfactants that may be adsorbed on the surface of the droplet. Surfactants can reduce the interfacial tension between a droplet and its surroundings, making it easier to deform the droplet and facilitating the slicing process.[23] Lower interfacial tension allows easier penetration of cutting tools and reduces the energy required to cut. Alternatively, the surfactant may form a protective layer on the surface of the droplet, effectively shielding it from direct contact with the cutting tool.[24] This may hinder the effectiveness of the cutting action and result in incomplete or non-uniform slices.

In our previous research work,[25] the LBM was used to numerically simulate a rising droplet being cut by a thin vertical surface (a knife). The study investigated the effect of simulation domain and grid resolution on droplet ascent, as well as symmetric and asymmetric cutting. The current paper builds on this work to explore in depth methods for effective control of droplet size and size distribution. Two different fluids are modelled by means of a phase field theory implemented in lattice Boltzmann.[26,27] The kinematic viscosities of the two fluids are identical and the density difference is accounted for as a body force only (Boussinesq approximation). The effect of grid resolution on droplet slicing is first verified and then the sensitivity of knife height, contact angle, rise velocity and deformation to boundary conditions is systematically discussed, as is the effect of two knives interacting with a single droplet. This simulation can help optimize the cutting process to achieve more accurate and consistent cuts. By carefully controlling the size of the droplets in the simulation, researchers can better understand the underlying physics of the droplet cutting process and develop more accurate models to predict the behaviour of real-world cutting processes.

2 | FLOW SYSTEM

This paper presents a numerical simulation of a rising droplet being cut by one or two vertical thin surfaces (knife). The simulations are two-dimensional with a buoyant circular drop released near the bottom of the domain and one or two knives located near the top of the domain (See Figure 1). Under the influence of gravity and buoyancy, the droplet begins to rise from rest and eventually reaches a stable ascent speed u. The droplet is then cut by the knife and the effect of the equilibrium contact angle and the use of one or two knives on the cutting of the droplet is investigated. Figure 1 also defines the coordinate system to be used throughout the paper.

In the fluid system, the density of fluid 1 is $\rho_d = 0.9 \times 10^3\,\mathrm{kg/m^3}$, and the kinematic viscosity is $\nu_d = 3.34 \times 10^{-6}\,\mathrm{m^2/s}$. The density of the fluid 2 is $\rho_c = 1 \times 10^3\,\mathrm{kg/m^3}$, and the kinematic viscosity is $\nu_c = 3.34 \times 10^{-6}\,\mathrm{m^2/s}$ (the subscripts d and c indicate the dispersed and continuous phases, respectively). The density difference between the droplet and the fluid is $\Delta\rho = \rho_c - \rho_d = 1 \times 10^2\,\mathrm{kg/m^3}$, with the dispersed phase being slightly lighter than the continuous phase. The surface tension between them is $\sigma = 1 \times 10^{-3}\,\mathrm{N/m}$.

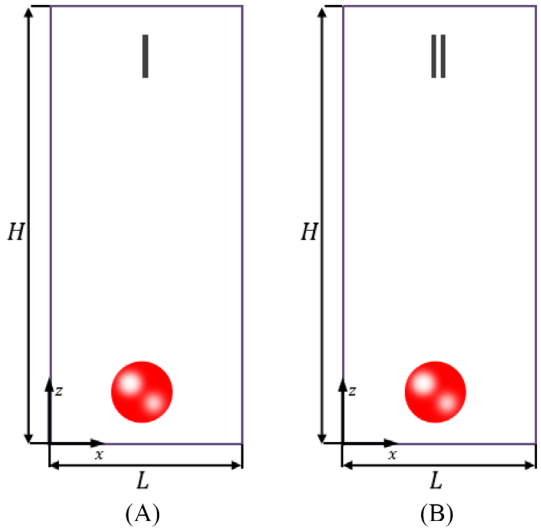

FIGURE 1 Schematic diagram of simulation domain and boundary conditions: The outer surface of the rectangular domain has periodic boundary conditions; all the boundaries of the knife are no-slip boundary conditions. At $t = 0$, the droplet is located at the centre near the bottom of the simulation domain and is circular. (A) One knife cutting a single rising droplet. (B) Two knives cutting a single rising droplet.

The equivalent diameter of the droplet volume is $d = (4S/\pi)^{1/2}$, where S is the area of the droplet. In the actual simulation, we refer to the data obtained by Clift et al.[28] through experiments to estimate the shape of the droplet and the stable rising speed u when the Eötvös (Eo) and Morton (Mo) numbers are given. We use a set of dimensionless parameters to determine the simulation system, where g is the acceleration due to gravity.

$$\text{Reynolds number: Re} = \frac{ud\rho_c}{\mu_c};$$

$$\text{Eötvös number: Eo} = \frac{g\Delta\rho d^2}{\sigma} = \frac{We\,|1-\lambda|}{Fr};$$

$$\text{Morton number: Mo} = \frac{g\Delta\rho\nu_c^4\rho_c^2}{\sigma^3} = \frac{g\Delta\rho\mu_c^4}{\rho_c^2\sigma^3};$$

$$\text{Weber number: We} = \frac{\rho_c u^2 d}{\sigma},\ \text{Froude number: Fr} = \frac{u^2}{gd};$$

$$\text{Density ratio: } \lambda = \frac{\rho_d}{\rho_c},\ \text{kinetic viscosity ratio: } \eta = \frac{\mu_d}{\mu_c}.$$

The Reynolds number determines the flow characteristics of viscous fluids. The Eötvös and Morton numbers are used to describe the shape of a droplet in moving fluids, with the Eötvös number being the ratio of buoyancy to surface tension and the Morton number being a constant for a given binary liquid system. The Weber number represents the ratio of inertial forces to surface tension effects, and the Froude number is a dimensionless parameter that characterizes the relative magnitudes of fluid inertia and gravity.

3 | NUMERICAL METHOD

3.1 | Governing equations

Phase field theory is the result of the further development of classical field theories such as van der Waals[29] and Cahn–Hilliard.[30,31] In phase field theory, the local state of matter at any point in time can be represented by a single variable called the order parameter $\varphi(\boldsymbol{r},t)$, which is a function of the position vector $\boldsymbol{r}$ and time t and is used to describe the state of the system. For binary liquid phase systems, the part related to phase transitions can be expressed as the free energy that is dependent on the order parameter $\varphi(\boldsymbol{r},t)$, which is represented as follows[32]:

$$F(\phi) = \int_V \left(\mathcal{F}(\varphi) + \frac{1}{2}k|\nabla\varphi|^2\right)dr, \tag{1}$$

Here, V represents the volume occupied by the system; $\frac{1}{2}k|\nabla\varphi|^2$ is the surface energy density, where k is a positive constant; $\mathcal{F}(\varphi)$ represents the bulk energy density, corresponding to the two phases of the fluid, each having two minimum values. The chemical potential μ_φ is defined as the variation of the free energy with respect to the order parameter φ:

$$\mu_\varphi = \frac{\delta F(\varphi)}{\delta\varphi} = \mathcal{F}'(\varphi) - k\nabla^2\varphi, \tag{2}$$

where $\mathcal{F}(\varphi) = d\mathcal{F}(\varphi)/d\varphi$. Van der Waals[29] assumed that the equilibrium interface profile can be obtained by minimizing $F(\varphi)$, that is, the equilibrium distribution satisfies $\mu_\varphi = \mathcal{F}'(\varphi) - k\nabla^2\varphi = 0$, which can be regarded as the controlling equation for the sequence parameter in equilibrium. The evolution of φ satisfies the following transport equation, which takes the following form[30,31,33,34]:

$$\frac{\partial\varphi}{\partial t} = M\nabla^2\mu - \boldsymbol{u}\cdot(\nabla\varphi), \tag{3}$$

where M is the mobility coefficient and $\boldsymbol{u}$ is the velocity field.

In the phase-field model, the interface between fluids is represented by a thin, finite transition region where

the fluids can mix. In each phase, the order parameter φ remains constant and changes continuously within the range of $[-1,1]$ in the finite transition region. For isothermal binary fluids (as in this study), φ represents the relative concentration of the two components.[30,35] This study employs continuity and momentum equations, combined with the convection–diffusion equation proposed by Cahn and Hilliard[30,31] to describe the fluid dynamics of this binary mixture (See Appendix A2).

3.2 | Free-energy lattice Boltzmann method

In 1995, Swift et al.[33] proposed an LBM called the free-energy lattice Boltzmann method to solve Equations (A1a) and (A1b). Based on the LBM, all system parameters in our study are expressed in lattice units [lu]. For the method used in this study, a uniform cubic mesh with a mesh spacing of Δx and a time step of Δt is adopted, where $c=\Delta x/\Delta t$ is the lattice velocity. The discrete velocity set is defined as $\mathbf{e}_{0-8}$.

$$\begin{pmatrix} e_{x0-8} \\ e_{z0-8} \end{pmatrix} = \begin{bmatrix} 0 & c & 0 & -c & 0 & c & -c & -c & c \\ 0 & 0 & c & 0 & -c & c & c & -c & -c \end{bmatrix},$$

The particle distribution functions $f(\boldsymbol{r},t)$ and $g(\boldsymbol{r},t)$ are used in this study, where $f(\boldsymbol{r},t)$ is used to solve the continuity Equation (A1a) and the Navier–Stokes Equation (A1b), and the fluid density and momentum are represented by $\rho=\sum_{i=0}^{8} f_i$ and $\rho\boldsymbol{u}=\sum_{i=0}^{8} f_i\boldsymbol{e}_i$ respectively. The function $g(\boldsymbol{r},t)$ is used to solve the convection–diffusion Equation (A1c), and represents the order parameter $\varphi=\sum_{i=0}^{8} g_i$ in the binary fluid system, where φ distinguishes the two fluids, with $\varphi=1$ in fluid 1 and $\varphi=-1$ in fluid 2, and $-1<\varphi<1$ at the interface between the two fluids, φ satisfying Equation (3). The model used in this study employs the single-relaxation-time collision operator (known as the Bhatnagar–Gross–Krook [BGK] model),[36] and the discrete lattice Boltzmann equations take the following form:

$$f_q\left(\boldsymbol{r}+\mathbf{e}_q\Delta t,t+\Delta t\right)=f_q(\boldsymbol{r},t)-\frac{f_q(\boldsymbol{r},t)-f_q^{eq}(\boldsymbol{r},t)}{\tau_f}+F_q, \tag{4}$$

$$g_q\left(\boldsymbol{r}+\mathbf{e}_q\Delta t,t+\Delta t\right)=g_q(\boldsymbol{r},t)-\frac{g_q(\boldsymbol{r},t)-g_q^{eq}(\boldsymbol{r},t)}{\tau_g}, \tag{5}$$

where the subscript q represents the discretized velocity direction; $f_q\left(\boldsymbol{r}+\mathbf{e}_q\Delta t,t+\Delta t\right)$ and $g_q\left(\boldsymbol{r}+\mathbf{e}_q\Delta t,t+\Delta t\right)$ represent the post-collision particle distribution functions, which represent the movement of particles from lattice site $(\boldsymbol{r},t)$ to neighbouring lattice site $\left(\boldsymbol{r}+\mathbf{e}_q\Delta t,t+\Delta t\right)$ along direction q; $f_q(\boldsymbol{r},t)$ and $g_q(\boldsymbol{r},t)$ are the pre-collision particle distribution functions; f_q^{eq} and g_q^{eq} represent the equilibrium distribution functions (see Appendix A2); $\mathbf{e}_q$ represents the discretized velocity in the q direction; τ_f and τ_g are dimensionless relaxation parameters; and F_q is the force acting on the particles. See Appendix A2 for details.

3.3 | Equilibrium contact angle

One focus of this paper is to simulate the cutting of rising liquid droplets on surfaces with different wettability. To vary the wettability properties of the cutting surface, the liquid–solid interaction parameter in the LBM model can be modified. This parameter determines the strength of the interaction between the fluid molecules and solid surfaces. By modifying this parameter, we can simulate different degrees of wettability of the cutting surface, from hydrophilic to hydrophobic properties.[37]

$$-\sqrt{\frac{2\kappa}{A}}\frac{\partial\varphi}{\partial n}=\left(\varphi^2-1\right)\cos\theta. \tag{6}$$

To achieve no-slip boundary conditions on the solid walls, the halfway bounce back rule was employed as the flow boundary condition. The equilibrium contact angle θ of the knife surface is related to the gradient in the normal direction of the order parameter φ on the solid surface $\frac{\partial\varphi}{\partial n}$. We use the following equilibrium boundary condition,[38] also referring to Appendix A2 for (κ and A).

In the simulation, we use a rectangular solid 'knife' to cut the liquid droplet. As shown in Figure 2, we apply boundary conditions at the surface of the knife and use the lattice points inside the knife to determine the normal derivative of the order parameter. At the vertical surface of the knife, we set $\frac{\partial\varphi}{\partial n}=\frac{\partial\varphi}{\partial x}$ and approximate the gradient as $\frac{\partial\varphi}{\partial n}\approx\frac{\varphi_e-\varphi_i}{\partial n}$, where $\Delta=1$. Based on the boundary conditions, we obtain the following:

$$\varphi_i=\varphi_e-\sqrt{\frac{A}{2\kappa}}\left(1-{\varphi_e}^2\right)\cos\theta \tag{7}$$

Equation (7) represents an approximate energy minimization that neglects some higher-order terms in the free energy; see the work of Lee and Lin[39] for details. This condition successfully creates an ideal equilibrium contact angle θ. For example, by setting $\varphi_i=\varphi_e$, we assume that $\cos\theta=0$, meaning we assume

that the surface of the knife has an equilibrium contact angle of $\theta = 90^{\circ}$. Therefore, through boundary conditions, we can study the influence of different equilibrium contact angles on droplet cutting.

4 | RESULTS

4.1 | Mesh resolution

Suitable dimensionless input parameters (Eo, Mo, λ, η) were determined based on a previous paper.[25] In the simulations presented in this paper, the lattice unit for a droplet with a diameter of 2.0 mm is represented by $\tilde{d} = 60$ [lu]. After determining the simulation system with Eo = 3.96, Mo = 1.24×10^{-4}, $\eta = 1$, and $\lambda = 0.90$, the simulation parameters are determined using the scaling factors in Appendix A3. The mesh step or linear scale factor $C_d = 3.33 \times 10^{-5}$ m, and the time step or scale factor of time $C_t = 6.05 \times 10^{-6}$ s.

The value of the droplet diameter $\tilde{d}$ represented by the lattice unit determines the mesh resolution, and its different conversion choices have a significant impact on the computational results and time aspects. Refer (again) to Appendix A3 that says that this $\sim$ symbol means a quantity in lattice units. To verify the effect of mesh resolution on the rising velocity Reynolds number and slicing process, we take a range of resolutions: $\tilde{d} = 36 - 96$ [lu] to represent $d = 2.0$ mm. When changing the physical length represented by the lattice unit, it is necessary to recalculate the simulation parameters. The numerical scaling factor f_m is set to change the droplet diameter $\tilde{d}f_m$ ($\tilde{d}_2 = f_m \tilde{d}_1, 0 < f_m$). On this basis, the values of Eo and Mo must be kept constant, while keeping the liquid viscosity constant $\widetilde{\mu_{c2}} = \widetilde{\mu_{c1}}$, $\widetilde{\mu_{d2}} = \widetilde{\mu_{d1}}$. All dimensionless parameters remain constant and the interface thickness is constant. The interface thickness ξ (see Appendix A3) is fixed at 1.14 [lu].[40]

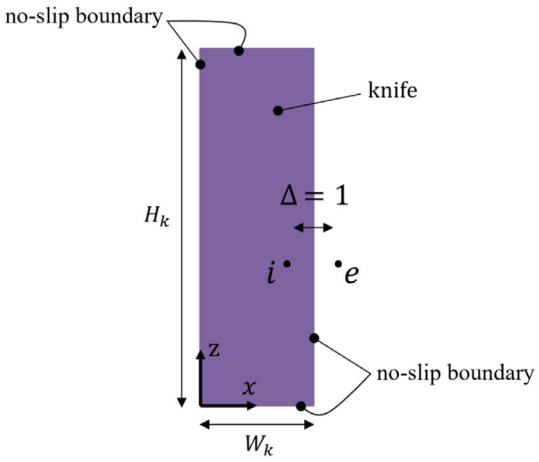

FIGURE 2 Schematic diagram of boundary conditions applied to the knife. On the right side of the knife, we show how we apply boundary conditions using the mesh point i inside the knife.

In this simulation, the parameters ($\tilde{\sigma}, \widetilde{\Delta\rho g}, \kappa$, A) were varied according to the droplet diameter $\tilde{d}$ with the numerical scaling factor f_m, using the formula for Eötvös and Morton numbers, while varying the simulation domain size (nx, nz). The simulation parameters are shown in Table 1.

Two sensitivity analyses were performed for the mesh resolution: mesh refinement ($f_m > 1.0$) and mesh coarsening ($0 < f_m < 1.0$). The blue dots in Figure 3 indicate the evolution of Reynolds number with dimensionless time for the original simulation condition droplet diameter $\tilde{d} = 60$. The dimensionless time $T_d = \frac{\tilde{t}_s \tilde{v}_c}{\tilde{d}^2}$, where $\tilde{t}_s$ is the current time step, and $\tilde{v}_c$ is the kinematic viscosity of the continuous phase (see Appendix A3). The dimensionless height of the knife $H_k = \tilde{H}_k/\tilde{d}$, and the dimensionless width of the knife $W_k = \tilde{W}_k/\tilde{d}$. Because H_k and W_k are dimensionless, the dimensions of the knife vary with the resolution in the lattice unit. The two-dimensional simulation domain is $20\tilde{d} \times 4\tilde{d}$. The equilibrium contact angle for the surface properties of the knife is 90°.

In the formula for calculating the rising velocity Reynolds number shown in Figure 3, where $u = \Delta z/\Delta t$, Δz being the distance travelled by the centre of the droplet during each time step calculated using the order

TABLE 1 f_m and other corresponding parameters for 2.0 mm diameter droplets representing different mesh resolutions in the simulation.

f_m[−]	$\tilde{d}$[lu]	$\tilde{\sigma}$[lu]	$\Delta\widetilde{\rho g}$[lu]	κ[lu]	A[lu]	nx[lu]	nz[lu]	Eo[−]	Mo[−]
0.6	36	1.66×10^{-3}	5.07×10^{-6}	1.42×10^{-3}	-2.186×10^{-3}	144	720	3.96	1.24×10^{-4}
0.8	48	1.245×10^{-3}	2.14×10^{-6}	1.065×10^{-3}	-1.639×10^{-3}	192	960	3.96	1.24×10^{-4}
1.0	60	1.00×10^{-3}	1.10×10^{-6}	0.855×10^{-3}	-1.316×10^{-3}	240	1200	3.96	1.24×10^{-4}
1.2	72	0.83×10^{-3}	6.34×10^{-7}	0.71×10^{-3}	-1.093×10^{-3}	288	1440	3.96	1.24×10^{-4}
1.4	84	0.712×10^{-3}	4.00×10^{-7}	0.609×10^{-3}	-0.937×10^{-3}	336	1680	3.96	1.24×10^{-4}
1.6	96	0.623×10^{-3}	2.68×10^{-7}	0.533×10^{-3}	-0.820×10^{-3}	384	1920	3.96	1.24×10^{-4}

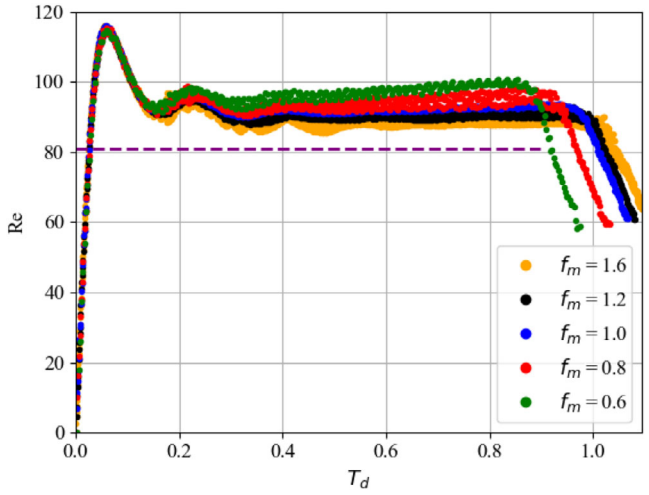

FIGURE 3 Evolution of Reynolds number at dimensionless time for simulated droplet ascent cutting at different mesh resolutions, Eo = 3.96, and Mo = 1.24×10^{-4}. Width of the knife $W_k = 0.167$, height of the knife $H_k = 0.517$. The dashed line in the figure is the Reynolds number reference value obtained by Bertakis et al.[41] at Eo = 3.40 and Mo = 1.22×10^{-6}. The end point of each time series is the moment when the droplet leaves the knife after it has been cut.

parameter φ. The range for calculating the Reynolds number is from the start of the droplet's ascent to when it is cut and leaves the knife. At the beginning, the droplet remains circular. This is followed by an accelerated ascent phase, where the droplet's rate of rise increases rapidly and the droplet appears deformed. As the droplet becomes flatter, the rate of ascent slows down, and a steady state is reached. After this, the droplet's rate of ascent decreases as it hits the knife. The droplet leaves the knife and completes the measurement of the rising velocity Reynolds number.

Based on the comparison between the original simulation and the mesh refinement, the droplets start to be cut at a relative deviation of 2.3%–4.3% of the time point. Therefore, the time deviation of the start of the cutting process is small and the original simulation ($f_m = 1.0$) can be used because it achieves a good balance between simulation accuracy and simulation time. We also perform a simulation check of mesh coarsening with the corresponding mesh step range $C_d = 4.16 \times 10^{-5} - 5.55 \times 10^{-5}$ m. The results show that the relative deviation of the dimensionless time for the droplet to start being cut falls by 4.8% between $\tilde{d} = 60$ [lu] and 48 [lu] and by 9.1% between $\tilde{d} = 60$ [lu] and 36 [lu]. By reducing the size of the simulation domain through mesh coarsening, the simulation time is reduced in the simulation, and the results obtained are generally consistent with the finer mesh. The deviation from the original simulation by mesh refinement and mesh coarsening is less than 10% in terms of the droplet rise Reynolds number at steady state.

In the experimental data of Bertakis et al.,[41] when the diameter of the liquid droplet was 2.0 mm and reached a stable state after rising, the Reynolds number was 81.0 (indicated by the dashed line in Figure 3). In our simulation, the discrepancy between the Reynolds number at the stable state reached under different mesh resolutions and the simulation results of Bertakis et al.[41] is less than 20%. It should be noted that our simulations are two-dimensional whereas the experiments are—obviously—three-dimensional, which likely explains the deviations observed.

4.2 | The effect of height of the knife

We need to make sure that the knife is sufficiently long so that it can complete the droplet cutting. The various parameters are in the row with $f_m = 1.0$ in Table 1. The surface equilibrium contact angle of the knife was 45°.

Here we study the effect of knife height and width on cutting droplets. In Figure 4, we show drop slicing scenarios for a range of knife heights and widths. The simulation results can be divided into four categories: (1) When using a knife with a small width and height, the drop is not cut by the knife (Figure 4C–E). (2) When the width of the knife is small and the height is large, the droplets are successfully cut into two parts while small droplets are formed eventually leave the knife. (Figure 4I). (3) When increasing the width of the knife, the droplets are able to be cut into two parts (Figure 4A,B,D,E,G,H). (4) When the width of the knife is large, the residual small droplets will adhere to the knife (Figure 4G,H).

To verify the effect of knife height on the cutting time, the dimensionless width of the knife was fixed at 0.167. At this width, the cutting of the droplet can be completed even if the height of the knife is small. The other simulation conditions were kept constant. We define four time points to better observe the process of the droplet being cut. (T_1) is the first contact between the droplet and the knife, where the first three-phase contact line is formed at the bottom of the knife. (T_2) is when the second three-phase contact line is formed at the bottom of the knife. (T_3) is when the first three-phase contact line leaves the knife. (T_4) is when the second three-phase contact line leaves the knife.

In Figure 5, we show the four time points T_1 to T_4 as a function of the height of the knife for a fixed equilibrium contact angle of 45° and for a knife width of $W_k = 0.167$. The location of the bottoms of the knives is all the same, and the droplet rises the same distance under the action of gravity and buoyancy. Therefore, as the droplet rises and is cut, the knife at different heights

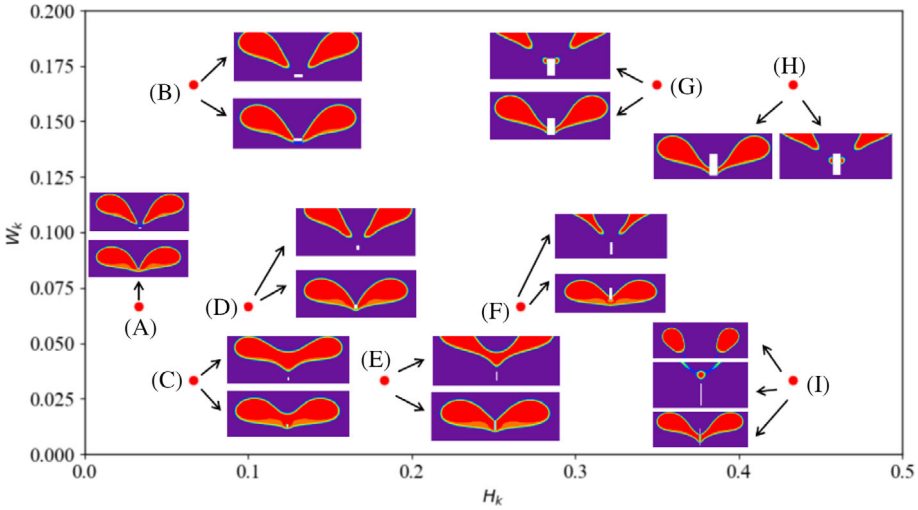

FIGURE 4 Cutting of droplets at different knife heights (H_k) and widths (W_k); H_k and W_k have been made dimensionless with the initial drop diameter. Each point shows an image of the state of the droplet during and after the cut. The equilibrium contact angle of the knife is 45°.

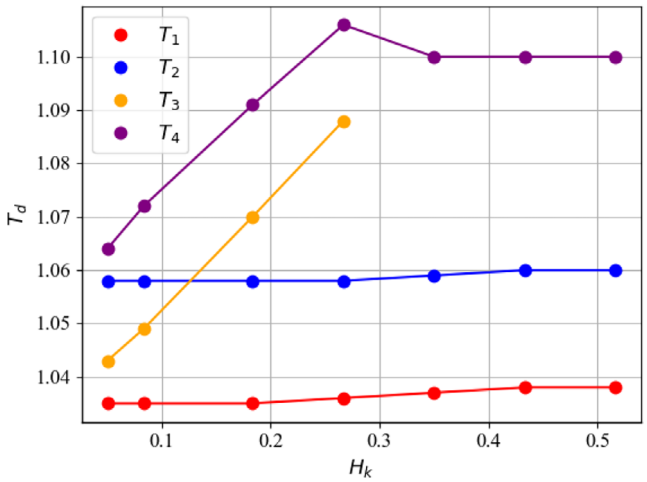

FIGURE 5 Time points of the three-phase contact line for droplets cut by knives of different heights. The width of the knife is $W_k = 0.167$. The equilibrium contact angle of the knife is 45°.

has the same time to form the first three-phase contact line and the second three-phase contact line between the droplet and the bottom of the knife. When the knife height is very small ($0.033 \le H_k \le 0.1$), the first three-phase contact line that is formed between the droplet and the knife will leave the knife before the second three-phase contact line is formed, and the droplet will be cut in the shortest time. When the knife height is ($0.183 \le H_k \le 0.267$), the first three-phase contact line formed at T_1 time point will leave the knife first, and after that, the droplet will continue to rise and be cut, and both three-phase contact lines will leave the knife. When the knife height is ($0.35 \le H_k$), neither of the two three-phase contact lines formed at times T_1 and T_2 reach the top of the knife. Due to the separation of the droplet and the small droplet adhered to the knife, both three-phase contact lines leave the knife simultaneously, resulting in the absence of a T_3 time point. As the height of the knife continues to increase, the position of the droplets separating from the small droplets adhering to the knife does not change, so the T_4 time point remains unchanged. Additionally, when the height of the knife is $H_k = 0.267$, the appearance of the T_4 time point occurs later than when the height of the knife is greater than $H_k > 0.267$. This is because during the cutting process of the droplet by the knife, the three-phase contact line formed at time T_1 disappears first due to the insufficient height of the knife and the influence of the equilibrium contact angle. The three-phase contact line formed at time T_2 disappears due to the separation of the droplet and the small droplet adhered to the knife.

4.3 | Contact angle

In this section, the effect of the equilibrium contact angle (θ_{eca}) of the knife on the slicing of the droplet will be investigated, and various parameters in Table 1 are used for the simulation system. The study includes the dynamic contact angles of droplets (advancing and receding contact angles), the droplet velocity after being cut at different equilibrium contact angles, as well as the droplet morphology and the droplet contact length with the knife when being cut. The advancing contact angle is measured from T_1 time point to T_3 time point; the receding contact angle is measured from T_2 time point to T_4 time point. The dynamic contact angles are determined by fitting the droplet profile to a tangent line taken at the intersection of the three-phase contact line. The value of the contact angle is affected by several factors, including the droplet velocity, the equilibrium contact angle of the knife, and the characteristics of the droplet itself

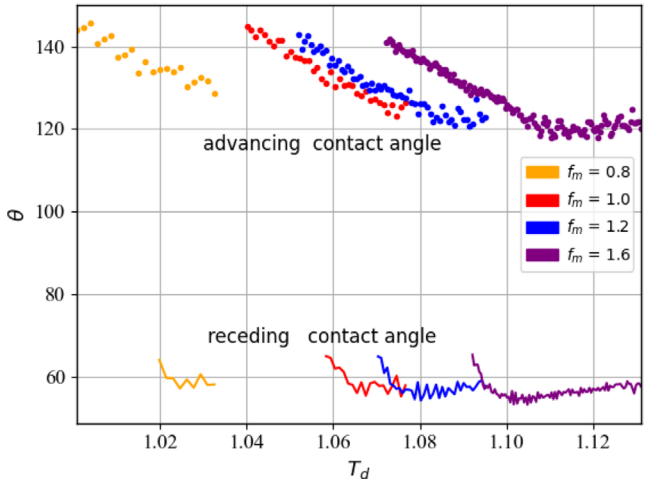

FIGURE 6 Evolution of the advancing and receding contact angles (θ) of droplets with time for different mesh resolutions at $\theta_{\text{eca}} = 90°$. The height of the knife $H_k = 0.517$, the width of the knife $W_k = 0.167$, and the droplet diameter $d = 2.0$ mm.

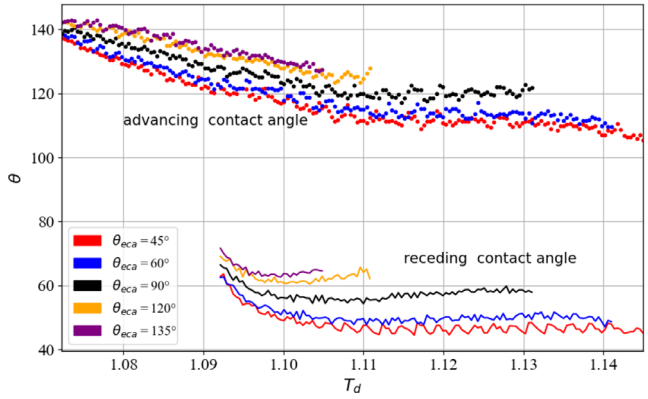

FIGURE 7 Evolution of the contact angle (θ) between the advancing and receding of the droplet with dimensionless time t for different equilibrium contact angles (θ_{eca}) with mesh resolution $f_m = 1.6$.

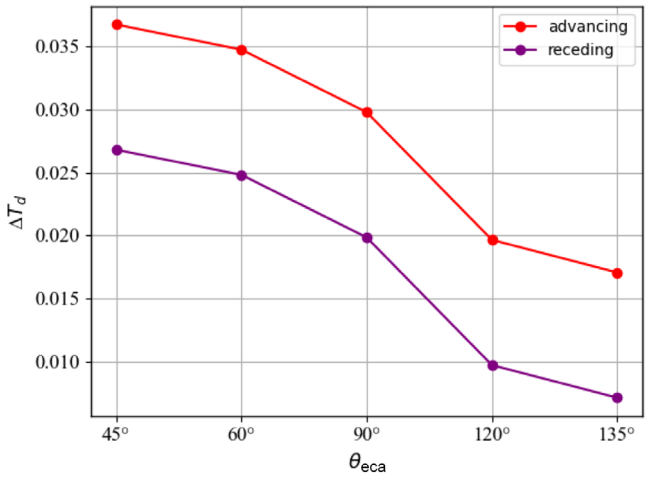

FIGURE 8 Variation of cutting time of droplets at different equilibrium contact angles for mesh resolution $f_m = 1.6$. The red part shows the cutting time for the advancing contact angle and the purple part shows the cutting time for the receding contact angle.

(viscosity and surface tension). Lee et al.[42] found that dynamic contact angles are usually higher than equilibrium contact angles and that statically wetted surfaces can become less wetted or even unwetted by dynamic droplet impact. During droplet cutting, the measured dynamic contact angle can differ from the equilibrium contact angle due to the complex interactions between these factors. The equilibrium contact angle is determined by the balance of intermolecular forces at the interface of the droplet in the static case. When the droplet is in motion, the droplet is rapidly deformed by the knife and subjected to high shear stresses, causing the contact angle of the droplet to change.

To verify the effect of mesh resolution on the dynamic contact angle, the variation of the advancing and receding contact angles when the droplet is cut by a knife with an equilibrium contact angle of 90° has been simulated with results shown in Figure 6 for four mesh resolutions in Table 1. As the mesh resolution increases, the value of the advancing and receding contact angle does not change much. Therefore, changing the mesh resolution has only a limited effect on the measurement of dynamic contact angles.

We expect that the larger the equilibrium contact angle, the easier the droplet is cut. Here we consider droplets cut on knives with different wettability levels, that is, hydrophilic and hydrophobic. The surface properties of the knife exhibit hydrophobicity when $\theta_{\text{eca}} > 90°$ and hydrophilicity when $\theta_{\text{eca}} < 90°$. The simulated system parameters are the ones with $f_m = 1.6$ in Table 1. The height of the knife $H_k = 0.85$ and the width $W_k = 0.167$. In Figure 7, the evolution of the contact angle on the advancing and receding of the droplet with time is shown to illustrate the differences between the five types of surfaces during the droplet cutting process. All simulation parameters are the same except for the equilibrium contact angle. If the equilibrium contact angle increases, the advancing and receding contact angles are slightly higher. Looking at the results of the droplet cutting times in Figure 8, ΔT_d is the length of time that the advancing and receding contact angles appear ($\Delta T_{da} = T_3 - T_1$ or $\Delta T_{dr} = T_4 - T_2$). It is clear that the advancing contact angle time ΔT_{da} is greater than the receding contact angle time ΔT_{dr} for the five surfaces. As the equilibrium contact angle increases, the cut lengths of the advancing and receding contact angles both decrease. In agreement with Son et al.,[43] the variation in the length of time a droplet is separated or cut is related to

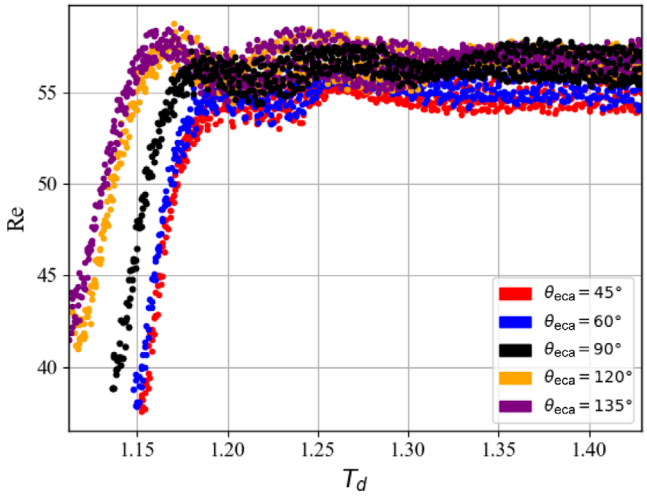

FIGURE 9 Evolution of Reynolds number with dimensionless time after T_4 time point for different equilibrium contact angles with mesh resolution $f_m = 1.6$.

the equilibrium contact angle; as the equilibrium contact angle increases, the shorter the contact time between the droplet and the surface of the rectangle or knife, and the easier it is for the droplet to separate away.

We now investigate the effect of equilibrium contact angle on the rising velocity Reynolds number of liquid droplets after the T_4 time point. We continue to simulate the motion of the cut droplet at different equilibrium contact angles with a mesh resolution of $f_m = 1.6$. The height of the knife is $H_k = 0.85$ and the width is $W_k = 0.167$. The droplet is cut equally into two parts and the Reynolds number formula is based on the droplet diameter is $\tilde{d}/\sqrt{2}$. As shown in Figure 9, after the two parts of the cut droplet leave the knife, the Reynolds number of the droplet quickly rises and then gradually stabilizes. As the equilibrium contact angle increases, the droplet leaves the knife earlier and the droplet appears less deformed (see Figure 10), the droplet has less contact area with the fluid, the droplet rises with less resistance and therefore leaves the knife with a slightly higher Reynolds number. After levelling off, there is a slight difference in the Reynolds number of the droplet continuing to rise after cutting at different equilibrium contact angles. At equilibrium contact angles $\theta_{eca} < 90°$, the droplet is cut by the knife with small droplets adhering to the knife. The volume of the two rising droplets is therefore reduced, and the Reynolds number of the continuing ascent velocity is slightly reduced. Some noise was found in the variation of the Reynolds number distribution of the droplet's continued rise velocity with dimensionless time. As the mesh resolution increases, the number of meshes in the simulation domain increases. The simulation becomes more sensitive

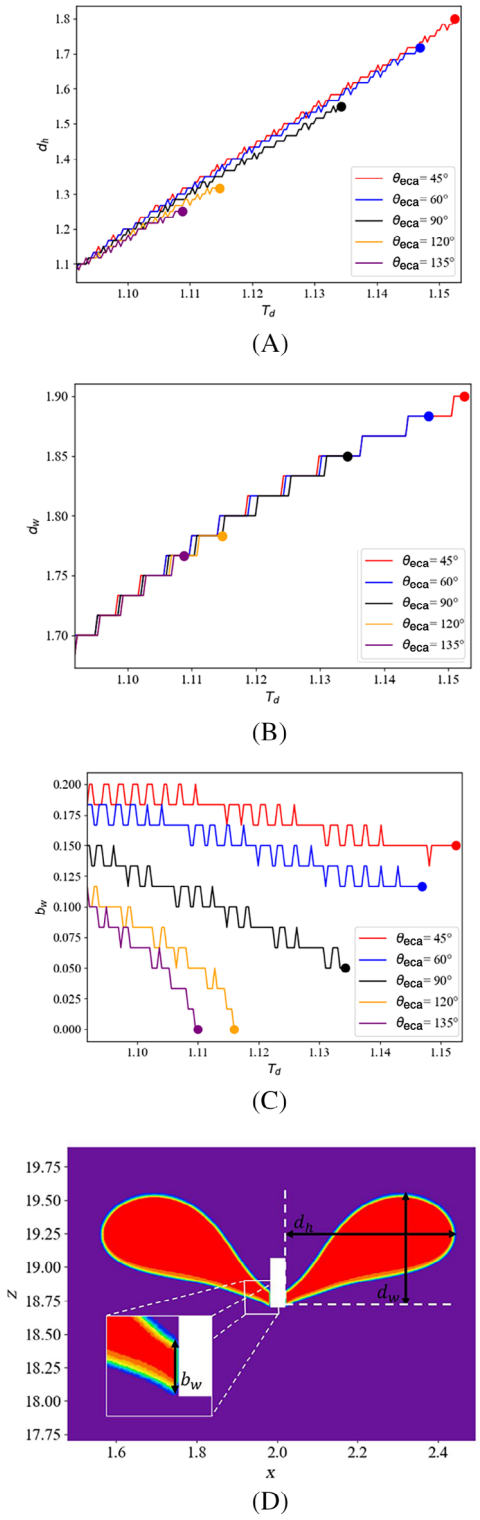

FIGURE 10 Evolution of droplet morphology and contact width with time for different equilibrium contact angles of droplets during the cutting process at a mesh resolution $f_m = 1.6$.
(A) Evolution of the droplet deformation height with time.
(B) Evolution of the droplet deformation width with time.
(C) Evolution of the contact width between the droplet and the knife with time. (D) Schematic diagram of the droplet deformation height (d_h), width (d_w), and contact width (b_w).

to small perturbations in the initial or boundary conditions, causing droplet velocity fluctuations.

We define the cutting process of the droplet in Figure 10 as the period between T_2 and the time point T_4. The asymmetry in the deformation of the droplet during the cutting process is more pronounced due to factors such as the surface characteristics of the knife, the droplet being cut by the knife and the rate of rise of the droplet. Figure 10A,B shows the evolution of the dimensionless height ($d_h = \tilde{d}_h/\tilde{d}$) and dimensionless width ($d_w = \tilde{d}_w/\tilde{d}$) of the droplet deformation with time. The larger the equilibrium contact angle, the smaller the increase in width and height of the droplet. The final height and width of the droplet deformation at the end of the cutting process are indicated by the points represented by the different equilibrium contact angle colours. Figure 10C shows the evolution of the dimensionless contact width ($b_w = \tilde{b}_w/\tilde{d}$) between the droplet and the knife during the cutting process as a function of time. During the droplet cutting process, when the surface property of the knife is hydrophobic, the contact width of the droplet and the knife decreases rapidly to 0, and there is no droplet residue on the surface of the knife. When the surface of the knife is hydrophilic, the contact width between the droplet and the knife is not reduced to 0. After the droplet has finished cutting and left the knife, a small droplet remains on the surface of the knife. Figure 10D shows a diagram of the droplet deformation height (d_h), width (d_w), and contact width (b_w), and x and z are coordinate systems and their values are dimensionless. x and z are scaled by the undeformed droplet diameter, where $x = \tilde{x}/\tilde{d}$, $z = \tilde{z}/\tilde{d}$. The lattice cells with order parameter $\varphi > 0$ are the lattice cells inside the droplet, and we use the φ filter to obtain the coordinates of all the positions of the lattice cells occupied by the droplet. The maximum and minimum values of the z-axis coordinates in the set of all coordinates are calculated to obtain d_h. The set of position coordinates of the x-axis coordinates out of the set of all coordinates is filtered out to be smaller than the x-axis of the knife, and the maximum and minimum values of the x-axis coordinates in the set are calculated to obtain d_w. The position coordinates of the knife are known, and the position coordinates of the droplets adjacent to the knife are calculated to obtain b_w. Due to discretization/grid effects in the plot of the dimensionless height, the dimensionless width and the dimensionless contact width as a function of time appear as steps.

Bakhshan et al.[44] studied the impact of liquid droplets on obstacles, considering three different surface conditions: hydrophilic ($\theta_{\text{eca}} = 45°$), neutral ($\theta_{\text{eca}} = 90°$), and hydrophobic ($\theta_{eca} = 135°$). The horizontal and vertical expansion trends of the droplets after impacting the different surfaces were found to be the same as in our simulations. The contact width between the droplet and the knife during the cutting process was as we observed. Table 2 shows a comparison between this paper and the simulated data of Bakhshan et al.[44] Time t and deformation height d_h are dimensionless. The time t for the droplet to leave the obstacle after impact and the deformation height of the droplet on the three different surfaces d_h. The expansion height of the droplet decreases as the equilibrium contact angle increases.

4.4 | Two knives interacting with a single droplet

In this section, we show results with two knives to cut through the rising droplets to see the different slices. The simulation system is according to Table 1 for $f_m = 1.0$, where $H_k = 0.517$ and $\theta_{\text{eca}} = 90°$. The state of the droplet when it is cut and the state of the cut part of the droplet was studied by varying the width of the two knives and the distance between the two knives ($k_d = \tilde{k}_d/\tilde{d}$). The situation before and after cutting is shown in Figure 11.

Two knives cut a droplet into three parts, with different slices for different knife widths and distances between the two knives. When cutting with the minimum knife distance and maximum knife width in the figure, the droplet is sliced into two parts, with no droplet in the middle part of the two knives (Figure 11A). By increasing the distance between the two knives and decreasing the width of the knife, the droplet was successfully cut into three parts, with the droplet in the parts on either side of the two knives continuing to rise and the droplet between the two knives remaining on the knife (Figure 11B–D). Afterwards, the width between the two knives is further increased and the droplet is cut, and the three parts of the droplet still coalesce into one

	$\theta_{\text{eca}} = 45°$		$\theta_{\text{eca}} = 90°$		$\theta_{\text{eca}} = 135°$	
	t	d_h	t	d_h	t	d_h
This paper	1.8	1.152	1.55	1.134	1.267	1.109
Bakhshan et al.[44]	2.88	2.2	<2.88	<1.65	<2.88	<1.5

TABLE 2 Comparison of the time t for a droplet to leave an obstacle and the deformation length d_h of a droplet after a simulated droplet impact on three different surfaces in this paper with Bakhshan et al.[44]

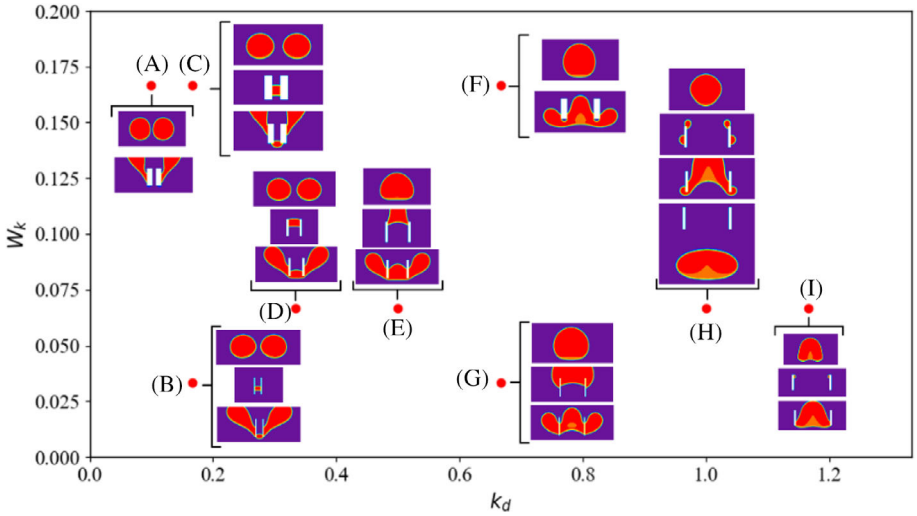

FIGURE 11 Different distances between two knives (k_d) and different widths (W_k) to simulate the cutting of a liquid drop. The height of the knife is $H_k = 0.517$. The equilibrium contact angle of the knife is $\theta_{eca} = 90°$.

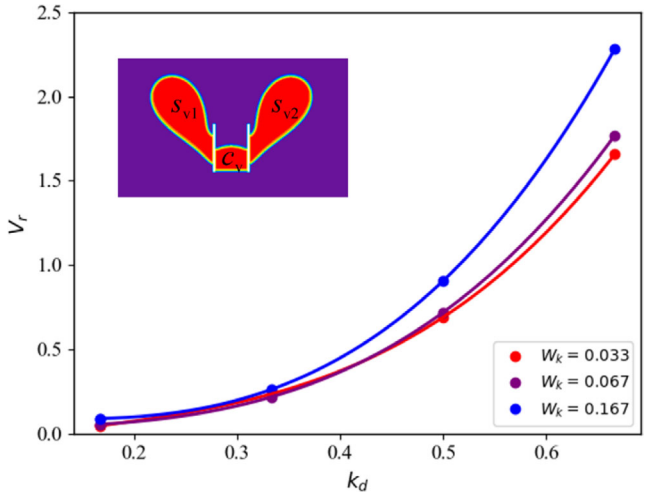

FIGURE 12 Volume ratios of cutting droplets for different knife widths and for different distances between the two knives. The height of the knife is $H_k = 0.517$. The equilibrium contact angle of the knife is $\theta_{eca} = 90°$. The dots represent individual simulations, and the curves are quadratic fits.

droplet and continue to rise (Figure 11F,G); when the width of the two knives is very large, the cut droplet remains on the knife (Figure 11H,I).

As shown in Figure 12, the droplet can be cut in three parts by two knives, the leftmost droplet of the two knives (s_{v1}), the rightmost droplet of the two knives (s_{v2}), and the droplet in the middle of the two knives (c_v). The volume ratio (V_r) is defined as follows:

$$V_r = \frac{c_v}{s_{v1}} \tag{8}$$

Given the left–right symmetry, the droplet volumes of s_{v1} and s_{v2} are equal. As expected, the volume ratio increases monotonically as the distance between the two knives increases. Increasing the width of the two knives, the volume ratio remains approximately unchanged when the distance between the two knives is small, and increases as the distance between the two knives increases.

5 | CONCLUSIONS

Based on the free energy lattice Boltzmann model, this paper studies the height of knife, contact angle, and the numerical simulation of two knives cutting a droplet as it rises. The simulation system parameters are determined for different resolutions using numerical scaling factors and scaling procedure. The equilibrium contact angle of the knife is achieved using the order parameter in the normal (vertical) direction of the solid surface.

In this study, the influence of mesh resolution on the start time of droplet cutting by the knife and the rising speed Reynolds number of the stable state is analysed by mesh coarsening and refinement analysis. For droplets with a diameter of 2.0 mm, the deviations from the original simulation in terms of droplet cutting start times were 9.1% and 4.3% for the coarsest and finest meshes obtained, respectively. The deviation from the original simulation by mesh refinement and coarsening is less than 10% when the droplet rise Reynolds number reaches a steady state. By varying the mesh resolution, the time at which the droplet starts to be cut and the steady state results of the rising Reynolds number deviate little from each other.

To investigate the effect of the knife height on droplet cutting, four time points are defined to observe the cutting process more effectively. By varying the height and width of the knife, it is possible to achieve a droplet that

is cut into one or two parts. Changing the height of the knife allows for no small droplets to remain after the droplets have been cut. The height of the knife affects the time it takes for the two three-phase contact lines to leave the knife. By reducing the height of the knife, the cutting time of the droplet is effectively reduced and the consumables for the knife are reduced.

We studied the effect of the knife's surface characteristics (i.e., equilibrium contact angle) on droplet slicing. The equilibrium contact angle affects the cutting time of the droplet and its shape changes. If the knife is hydrophobic, the cutting time of the droplet is relatively short, the length and width changes of the droplet are small, and there is no residue of small droplets on the knife. If the knife is hydrophilic, the cutting time of the droplet is long, the length and width changes of the droplet are significant, and there is a residual droplet on the knife. The size of the droplets remaining on the knife after the droplets have been cut by a knife with different surface characteristics varies, making the final droplets smaller in size. As a result, there is a slight difference in the droplet's continued rise rate after the Reynolds number has reached stability.

In the numerical simulation of cutting droplets with two knives, we observed a series of cutting situations. By controlling the distance between the two knives while keeping their width constant, the cutting of the droplet into three parts can be achieved, and the middle part of the droplet will remain between the two knives. Simultaneously controlling the distance between two knives, the droplets will be cut into two parts or coalesce into one droplet after cutting. Increasing the distance between the two knives increases the volume ratio of the droplet.

In this simulation study, some findings and insights were obtained on the control of droplet size by varying the height of the knife, contact angle, and using two knives. This may provide some guidance for the design of microchannel technology and spray application in related applications such as droplet size control. The research in this paper is based on simulations carried out in two dimensions. For the time being, no in-depth research has been carried out on the three-dimensional, real-life droplet rise and cut problem. In order to provide a more accurate description of the actual flow problems in engineering, we will carry out future research on the three-dimensional droplet rise and cut problem. In the simulation of using two knives to cut the droplets, the middle part of the droplet stays between the two knives. In the next stage of the work, we plan to achieve the continued upward movement of the middle part of the droplet after being cut by changing the knife (height and shape) and the surface characteristics of the knife. Our current work separately investigates the effects of knife size and contact angle on cutting behaviour. Future work considering their combined effect on the slicing process may be interesting in order to obtain a more general study that will eventually provide correlations in terms of cutting time. Currently, only one droplet is used in the simulation to be cut by the knife, and the impact of residual droplets on the next droplet cutting cannot be determined. Therefore, in the next stage of the work, we will set a larger simulation domain, release multiple droplets to achieve continuous cutting, and study the impact of residual droplets on droplet cutting. The properties of the droplets and the stable velocity of the droplets after rising are also important factors that affect cutting and can be compared and studied for different parameter impacts in the future.

NOMENCLATURE

A, κ	parameters connected with surface tension and interface thickness
b_w	(dimensionless) contact width
$\tilde{b_w}$	contact width ([lu])
C	scaling factor
c_s^2	speed of sound squared in lattice units (m^2/s^2)
d	equivalent diameter (mm)
$\tilde{d}$	equivalent drop diameter in lattice units ([lu])
d_h	(dimensionless) droplet deformation height
$\tilde{d_h}$	droplet deformation height ([lu])
d_w	(dimensionless) droplet deformation width
$\tilde{d_w}$	droplet deformation width ([lu])
e_{aq}	discrete velocity (mm/s)
Eo	(dimensionless) Eötvös number
f_m	a factor (when changing the drop diameter d)
$f_q^{\mathrm{eq}}, g_q^{\mathrm{eq}}$	discrete Maxwell–Boltzmann distributions (or equilibrium distributions)
$F(\phi)$	free energy functional
$f(\boldsymbol{r},t), g(\boldsymbol{r},t)$	particle distribution functions
F_q	forcing term ($F_q = \mathrm{g}\Delta\rho, \mathrm{N}$)
$\mathcal{F}(\varphi)$	the bulk energy density
Fr	(dimensionless) Froude number
g	gravitational acceleration (m^2/s)
H_k	(dimensionless) height of the knife
$\tilde{H_k}$	height of the knife ([lu])
k_d	(dimensionless) distance between two knives
$\tilde{k_d}$	distance between two knives ([lu])
M	mobility parameter
Mo	(dimensionless) Morton number
p_0	bulk pressure (Pa)
$P_{\alpha\beta}$	full pressure tensor (Pa)
$P_{\alpha\beta}^{\mathrm{chem}}$	'chemical' pressure tensor (Pa)
$P_{\alpha\beta}^{th}$	'thermodynamic' pressure tensor (Pa)

Re	(dimensionless) Reynolds number
$\tilde{t}_s$	the current time step ([lu])
T_d	dimensionless time
V_r	droplet volume ratio
W_k	(dimensionless) width of the knife
$\tilde{W}_k$	width of the knife ([lu])
We	(dimensionless) Weber number
θ_{eca}	equilibrium contact angle (°)
τ_f, τ_g	dimensionless relaxation parameters
ω_q	weight coefficients
$\sim$	parameters in lattice units
$\Delta\rho$	density difference (kg/m^3)
q	discretized velocity direction
t	time (s)
u	rising velocity (mm/s)
$\boldsymbol{r}$	position vector (mm/s)
Γ	coefficient of mobility
Δt	time step (s)
Δx	mesh step (mm)
η	dynamic viscosity ratio
θ	contact angle (degree)
λ	density ratio
μ	dynamic viscosity (Pa s)
$\mu(\varphi)$	chemical potential (Pa)
ν	kinematic viscosity (m^2/s)
ξ	diffuse interface ([lu])
ρ	density (kg/m^3)
σ	interfacial tension (N/m)
φ	order parameter of phase field

AUTHOR CONTRIBUTIONS

Jiawei Cao: Data curation; investigation; methodology; writing – original draft. **Fengjiao Liu:** Project administration; resources; supervision; validation; writing – review and editing. **Shipeng Wang:** Investigation; validation; writing – original draft. **Xiang Li:** Investigation; methodology; validation; writing – original draft. **Lijuan Zhang:** Investigation; methodology; writing – original draft. **Jie Lu:** Resources; supervision; writing – review and editing. **Jos J. Derksen:** Project administration; software; supervision; writing – review and editing.

ACKNOWLEDGEMENTS

This work was supported by the National Natural Science Foundation of China (Nos. 22078191, 21978165, and 92156020), Shanghai Sailing Program (No. 20YF1416000), and SUES High-End Foreign Experts Recruitment Program.

PEER REVIEW

The peer review history for this article is available at https://www.webofscience.com/api/gateway/wos/peer-review/10.1002/cjce.25066.

DATA AVAILABILITY STATEMENT

The authors confirm that the data supporting the findings of this study are available within the article.

ORCID

Fengjiao Liu https://orcid.org/0000-0002-2039-4786

REFERENCES

[1] S. M. Cunningham, D. A. Tanner, *Int. J. Environ. Res. Public Health.* **2020**, *17*, 15.
[2] S. Madlmeir, T. Forgber, M. Trogrlic, D. Jajcevic, A. Kape, L. Contreras, A. Carmody, P. Liu, C. Davies, A. Sarkar, J. G. Khinast, *Chem. Eng. Sci.* **2022**, *252*, 16.
[3] L. Xun, F. Garcia-Ruiz, F. X. Fabregas, E. Gil, *Sci. Total Environ.* **2022**, *826*, 15.
[4] C. Cheng, C. Alex Chang, J. A. Yeh, *Opt. Express* **2006**, *14*, 4101.
[5] K. A. Raman, R. K. Jaiman, T. S. Lee, H. T. Low, *Int. J. Heat Mass Transfer* **2016**, *95*, 336.
[6] M. Tembely, D. Vadillo, A. Soucemarianadin, A. Dolatabadi, *Processes* **2019**, *7*, 12.
[7] S. E. M. Tilehboni, E. Fattahi, H. H. Afrouzi, M. Farhadi, *J. Mol. Liq.* **2015**, *212*, 544.
[8] R. Ma, X. Zhou, B. Dong, W. Li, J. Gong, *Int. J. Heat Fluid Flow* **2018**, *71*, 1.
[9] J. Liang, M. Gao, L. Chen, D. Wang, Z. Wang, *Comput. Fluids* **2022**, *248*, 105674.
[10] A. A. Abubakar, B. S. Yilbas, G. Hassan, H. Al-Qahtani, H. Ali, A. Al-Sharafi, *J. Fluids Eng.* **2020**, *142*, 10.
[11] X. H. Liu, Y. M. Zhao, S. Chen, S. Q. Shen, X. Y. Zhao, *Phys. Fluids* **2017**, *29*, 9.
[12] P. T. Naveen, R. R. Simhadri, S. K. Ranjith, *Fluid. Dyn.* **2020**, *55*, 640.
[13] J. Alinejad, M. M. Peiravi, *Meccanica* **2020**, *55*, 1975.
[14] Y. L. Wang, D. Q. Minh, G. Amberg, *J. Non-Newtonian Fluid Mech.* **2017**, *243*, 38.
[15] A. S. Ellis, F. T. Smith, A. H. White, *Q. J. Mech. Appl. Math.* **2011**, *64*, 107.
[16] S. Q. Shen, F. F. Bi, Y. L. Guo, *Int. J. Heat Mass Transfer* **2012**, *55*, 6938.
[17] M. C. Jiang, B. Zhou, *Int. J. Hydrogen Energy* **2020**, *45*, 29848.
[18] D. A. Bolleddula, A. Berchielli, A. Aliseda, *Adv. Colloid Interface Sci.* **2010**, *159*, 144.
[19] C. Y. Lim, Y. C. Lam, *Microfluid. Nanofluid.* **2014**, *17*, 131.
[20] P. K. Unnikrishnan, V. Vaikuntanathan, D. Sivakumar, *Colloids Surf., A* **2014**, *459*, 109.
[21] S. Herbert, S. Fischer, T. Gambaryan-Roisman, P. Stephan, *Int. J. Heat Mass Transfer* **2013**, *61*, 605.
[22] W. Y. Yu, M. K. Wang, F. F. Wang, X. W. S. Wang, B. L. Wu, *Appl. Phys. A: Mater. Sci. Process.* **2022**, *128*, 13.
[23] D. Y. Li, A. Buffo, W. Podgorska, D. L. Marchisio, Z. M. Gao, *Chin. J. Chem. Eng.* **2017**, *25*, 1369.
[24] N. Shardt, M. B. Bigdeli, J. A. W. Elliott, P. A. Tsai, *J. Phys. Chem. Lett.* **2019**, *10*, 7510.
[25] Z. Y. Lu, F. J. Liu, X. J. Liu, L. J. Zhang, H. K. Yuan, J. Lu, J. J. Derksen, *Can. J. Chem. Eng.* **2022**, *100*, S327.
[26] Y. Q. Zu, S. He, *Phys. Rev. E* **2013**, *87*, 23.
[27] J. Kim, *Comput. Phys. Commun.* **2012**, *12*, 613.

[28] R. Clift, J. R. Grace, M. E. Weber, *Bubbles, Drops, and Particles*, Dover Publications, New York **1978**.
[29] J. S. Rowlinson, *J. Stat. Phys.* **1979**, *20*, 197.
[30] J. W. Cahn, J. E. Hilliard, *J. Chem Phys.* **1958**, *28*, 258.
[31] J. W. Cahn, J. E. Hilliard, *J. Chem Phys.* **1959**, *31*, 688.
[32] O. Penrose, P. C. Fife, *Phys. D* **1990**, *43*, 44.
[33] M. R. Swift, E. Orlandini, W. R. Osborn, J. M. Yeomans, *Phys. Rev. E* **1996**, *54*, 5041.
[34] A. J. Bray, *Phys. A* **1995**, *194*, 41.
[35] V. E. Badalassi, H. D. Ceniceros, S. Banerjee, *J. Comput. Phys.* **2003**, *190*, 371.
[36] P. L. Bhatnagar, E. P. Gross, M. Krook, *Phys. Rev. E* **1954**, *94*, 511.
[37] D. Khojasteh, M. K. D. Manshadi, S. M. Mousavi, F. Sotoudeh, R. Kamali, A. Bordbar, *J. Braz. Soc. Mech. Sci. Eng.* **2020**, *42*, 11.
[38] H. Liu, A. J. Valocchi, Y. Zhang, Q. Kang, *J. Comput. Phys.* **2014**, *256*, 334.
[39] T. Lee, L. Lin, *J. Comput. Phys.* **2010**, *229*, 8045.
[40] V. M. Kendon, M. E. Cates, I. Pagonabarraga, J.-C. Desplat, P. Bladon, *J. Fluid Mech.* **2001**, *440*, 147.
[41] E. Bertakis, S. Gro, J. Grande, O. Fortmeier, A. Reusken, A. Pfennig, *Chem. Eng. Sci.* **2010**, *65*, 2037.
[42] J. B. Lee, D. Derome, R. Guyer, J. Carmeliet, *Langmuir* **2016**, *32*, 1299.
[43] S. W. Son, C. H. Jeong, M. Ha, H. R. Kim, *Comput. Fluids* **2014**, *105*, 294.
[44] M. Bakhshan, M. Worner, A. Dadvand, *Computational Particle Mechanics* **2021**, *8*, 973.
[45] A. Vorobev, *Phys. Rev. E* **2010**, *82*, 056312.
[46] H. Kusumaatmaja, *PhD Thesis*. University of Oxford **2008**.
[47] T. Krüger, H. Kusumaatmaja, A. Kuzmin, O. Shardt, G. Silva, E. M. Viggen, *The Lattice Boltzmann Method – Principles and Practice*, Springer Publishing, New York **2016**.

How to cite this article: J. Cao, F. Liu, S. Wang, X. Li, L. Zhang, J. Lu, J. J. Derksen, *Can. J. Chem. Eng.* **2023**, 1. https://doi.org/10.1002/cjce.25066

APPENDIX A

A1 | Phase field description of a binary fluid system

The phase-field model is only applicable to fluids with small density differences. In this study, the relative density difference between the two liquids is only 10%, so the Boussinesq approximation[45] is used to determine the net gravity. For the present system, the hydrodynamics of this binary mixture are described as follows:

$$\partial_t \rho + \partial_\alpha(\rho u_\alpha) = 0, \tag{A1a}$$

$$\partial_t(\rho u_\alpha) + \partial_\beta(\rho u_\alpha u_\beta) = -\partial_\beta P^{th}_{\alpha\beta} + \partial_\beta \nu(\rho\partial_\alpha u_\beta + \rho\partial_\beta u_\alpha) + g\Delta\rho, \tag{A1b}$$

$$\partial_t \varphi + \partial_\alpha(\varphi u_\alpha) = M\partial^2_{\beta\beta}\mu, \tag{A1c}$$

Here, ρ is the density, the kinematic viscosity of the mixture is ν, and the subscripts α represent the Cartesian directions x, y, and z. u_α is the velocity field. μ is the chemical potential (see Equation 2). A symmetric double well potential is used to describe the phase separation.

$$V = \frac{A}{2}\varphi^2 + \frac{B}{4}\varphi^4. \tag{A2}$$

The chemical potential μ in Equation (2) is defined as follows[40]:

$$\mu(\varphi) = A\varphi - A\varphi^3 - \kappa\partial^2_{\alpha\alpha}\varphi, \tag{A3}$$

Here, A is a parameter of the free energy model with A value less than 0, and A and κ are parameters related to surface tension and interface thickness.

$P^{th}_{\alpha\beta}$ represents the 'thermodynamic' pressure tensor, which includes two parts[40]: an isotropic contribution $P\delta_{\alpha\beta}$ to describe the pressure of ideal gas, and the other part is the 'chemical' pressure tensor $P^{\text{chem}}_{\alpha\beta}$ defined as follows:

$$P^{\text{chem}}_{\alpha\beta} = \delta_{\alpha\beta}\left[\varphi\frac{\delta V}{\delta\varphi} - \mathrm{V} - \kappa\left\{\varphi\partial^2_{yy}\varphi + \frac{1}{2}|\partial_\alpha\varphi|^2\right\}\right] + \kappa(\partial_\alpha\varphi)(\partial_\beta\varphi). \tag{A4}$$

A2 | Lattice Boltzmann method and parameters

The discrete Equations (4) and (5) can be solved in two steps: collision step and streaming step.

$$\text{Collision step: } f'_q(\boldsymbol{r},t) = f_q(\boldsymbol{r},t) - \frac{1}{\tau_f}\left[f_q - f^{eq}_q\right] + F_q$$

$$g'_q(\boldsymbol{r},t) = g_q(\boldsymbol{r},t) - \frac{1}{\tau_g}\left[g_q - g^{eq}_q\right] \tag{A5}$$

$$\text{Streaming step: } f_q(\boldsymbol{r}+\mathbf{e}_q\Delta t, t+\Delta t) = f'_q(\boldsymbol{r},t)$$

$$g_q(\boldsymbol{r}+\mathbf{e}_q\Delta t, t+\Delta t) = g'_q(\boldsymbol{r},t) \tag{A6}$$

The forcing term is incorporated as follows:

$$F_q = \omega_q(\boldsymbol{e}_q\cdot\boldsymbol{F}), \tag{A7}$$

where $\boldsymbol{F}$ is the macroscopic force and ω_q is the weighting factor[46]:

$$\omega_{1-6}=\frac{1}{6},\ \omega_{7-18}=\frac{1}{12},$$

$$\omega_{1-2}^{xx}=\omega_{3-4}^{yy}=\omega_{5-6}^{zz}=\frac{5}{12},\ \omega_{3-6}^{xx}=\omega_{1-2,5-6}^{yy}=\omega_{1-4}^{zz}=-\frac{1}{3},$$

$$\omega_{7-10}^{xx}=\omega_{15-18}^{xx}=\omega_{7-14}^{yy}=\omega_{11-18}^{zz}=-\frac{1}{24},$$

$$\omega_{11-14}^{xx}=\omega_{15-18}^{yy}=\omega_{7-10}^{zz}=\frac{1}{12}, \tag{A8}$$

$$\omega_{1-6}^{xy}=\omega_{1-6}^{yz}=\omega_{1-6}^{zx}=0,\ \omega_{7,10}^{xy}=\omega_{11,14}^{yz}=\omega_{15,18}^{zx}=\frac{1}{4},$$

$$\omega_{8-9}^{xy}=\omega_{12-13}^{yz}=\omega_{16-17}^{zx}=-\frac{1}{4},\ \omega_{11-18}^{xy}=\omega_{7-10}^{yz}=\omega_{7-14}^{zx}=0.$$

For equilibrium distribution functions f_q^{eq} and g_q^{eq} for $1\le q\le 18$, the following equations are used[46]:

$$f_q^{eq}=\frac{\omega_q}{c^2}\left(p_0-\kappa\varphi\left(\partial_{xx}^2+\partial_{yy}^2+\partial_{zz}^2\right)+e_{\alpha q}\rho u_\alpha+\frac{3}{2c^2}\left[e_{\alpha q}e_{\beta q}-\frac{c^2}{3}\delta_{\alpha\beta}\right]\rho u_\alpha u_\beta\right.$$
$$\left.+\frac{\kappa}{c^2}\left(\omega_q^{xx}\partial_x\varphi\partial_x\varphi+\omega_q^{yy}\partial_y\varphi\partial_y\varphi+\omega_q^{zz}\partial_z\varphi\partial_z\varphi+\omega_q^{xy}\partial_x\varphi\partial_y\varphi+\omega_q^{xz}\partial_x\varphi\partial_z\varphi+\omega_q^{yz}\partial_y\varphi\partial_z\varphi\right)\right) \tag{A9a}$$

$$g_q^{eq}=\frac{\omega_q}{c^2}\left(\Gamma\mu+\boldsymbol{e}_{\alpha q}\rho u_\alpha+\frac{3}{2c^2}\left[\boldsymbol{e}_{\alpha q}\boldsymbol{e}_{\beta q}-\frac{3}{c^2}\delta_{\alpha\beta}\right]\varphi u_\alpha u_\beta\right) \tag{A9b}$$

and the equilibrium distribution function at $q=0$ is as follows:

$$f_0^{eq}=\rho-\sum\nolimits_{q=1}^{Q-1}f_q^{eq}, \tag{A10a}$$

$$g_0^{eq}=\varphi-\sum\nolimits_{q=1}^{Q-1}g_q^{eq}. \tag{A10b}$$

For a two-phase interface, the value of φ is determined by the following equation:

$$\varphi(x)=\varphi_0 tanh\frac{x}{\xi}, \tag{A11}$$

φ is the value of the order parameter at the interface of the two phases. φ_0 is the order parameter value in the bulk of the two phases, $\varphi_0=1$.

The thickness ξ of the two-phase interface is given by the following:

$$\xi=\left(\frac{2\kappa}{-A}\right)^{\frac{1}{2}}. \tag{A12}$$

The surface tension σ follows the equation:

$$\sigma=\frac{4}{3}\kappa\frac{\varphi_0^2}{\xi}. \tag{A13}$$

The local density ρ, the local momentum $\rho\boldsymbol{u}$, and the local order parameter φ of the fluid at a single lattice point are the result of summing over all directions q:

$$\sum_q f_q=\rho, \tag{A14a}$$

$$\sum_q \boldsymbol{e}_q f_q=\rho\boldsymbol{u}+\frac{\Delta t}{2}\boldsymbol{F}, \tag{A14b}$$

$$\sum_q g_q=\varphi. \tag{A14c}$$

The pressure p_0 in Equations (A9a) and (A9b) is calculated as follows:

$$p_0=c_s^2\rho+\frac{A}{2}\varphi^2-\frac{3A}{4}\varphi^4 \tag{A15}$$

τ_f is determined by the kinematic viscosity of the mixture:

$$\tau_f(\varphi)=\frac{\nu(\varphi)}{c_s^2\Delta t}+\frac{1}{2} \tag{A16}$$

The kinematic viscosity ν of the mixed liquid is expressed as a function of the order parameter φ:

$$v(\varphi) = v_c \frac{1-\varphi}{2} + v_d \frac{1+\varphi}{2} \tag{A17}$$

v_c and v_d are the kinematic viscosities of the continuous and dispersed phases, respectively.

The mobility M, the flow coefficient Γ, and the relaxation parameter τ_g are related by the following equation[47]:

$$M = \Delta t \Gamma \left(\tau_g - \frac{1}{2}\right) \tag{A18}$$

The mobility M is determined by the flow coefficient Γ, where $c_s^2 = \frac{1}{3}$, which represents the square of the speed of sound in the lattice unit.

A3 | Scaling procedure

Numerical simulations based on the lattice Boltzmann method require the correct matching of lattice units to physical units and numerical systems, which can be achieved by using a proportionality factor. By equating the physical and lattice dimensions, the value of the proportionality factor can be obtained. In this study, the symbol $\sim$ is used to indicate that this parameter is expressed in lattice units. Using Equation (A13), the formula for κ is obtained:

$$\kappa = \frac{3\xi}{4\varphi_0^2} \frac{\sigma}{C_\sigma} \# \tag{A19}$$

Here, after κ has been determined, the value of A can be calculated by Equation (A12). $\varphi_0 = 1$ and C_σ is scale factor for surface tension, whose scale factor can be written as follows:

$$C_\sigma = \frac{\sigma}{\tilde{\sigma}} \tag{A20}$$

The Boussinesq approximation[45] states that if the density difference is much smaller than the density of the two actual liquids, then density variations only play a role in the force $\Delta\rho g$. The proportionality factor for the force is determined by the definition of the Eötvös number ($\mathrm{Eo} = g\Delta\rho d^2/\sigma$):

$$\Delta\tilde{\rho} g = \frac{\tilde{\sigma}}{\tilde{d}^2} \mathrm{Eo} \tag{A21}$$

where $\tilde{\sigma}$ can be obtained from Equation (A20) and $\tilde{d}$ denotes the diameter of the droplet in the lattice unit.

The dynamic viscosities of the continuous and dispersed phases were determined from the definition of the Morton number $\left(\mathrm{Mo} = \left(g\Delta\rho\mu_c^4\right)/\left(\rho_c^2\sigma^3\right)\right)$ and the viscosity ratio η ($\eta = \mu_d/\mu_c$):

$$\tilde{\mu_c} = \left(\tilde{\rho}_c^2 \tilde{\sigma}^2 \tilde{d}^2 \frac{Mo}{Eo}\right)^{1/4} \tilde{\mu_d} = \eta \tilde{\mu_c} \tag{A22}$$

The kinematic viscosity is as follows:

$$\tilde{\nu_c} = \frac{\tilde{\mu_c}}{\tilde{\rho_c}} \tilde{\nu_d} = \frac{\tilde{\mu_d}}{\tilde{\rho_d}} \tag{A23}$$

We therefore introduce the following scale factors:

$$\begin{aligned} &\text{Density: } C_\rho = \frac{\rho}{\tilde{\rho}}; \\ &\text{Kinematic viscosity: } C_\nu = \frac{\nu_c}{\tilde{\nu_c}}; \\ &\text{Force: } C_{force} = \frac{\Delta\rho g}{\Delta\tilde{\rho} g}. \end{aligned} \tag{A24}$$

Using the definitions of the Froude number ($\mathrm{Fr} = u^2/gd$), Reynolds number ($\mathrm{Re} = ud\rho_c/\mu_c$) and Weber number ($\mathrm{We} = \rho_c u^2 d/\sigma$), and the above scaling factors, the scaling factors for velocity, length and time can be determined as follows:

$$\begin{aligned} &\text{Length: } C_d = \frac{C_\nu^2 C_\rho}{C_\sigma}; \\ &\text{Velocity: } C_u = \frac{C_\sigma}{C_\nu C_\rho}; \\ &\text{Time: } C_t = \frac{C_\nu^3 C_\rho^2}{C_\sigma^2}; \end{aligned} \tag{A25}$$